Research Article

Younghwan Yang, Hongyoon Kim, Trevon Badloe and Junsuk Rho*

Gap-plasmon-driven spin angular momentum selection of chiral metasurfaces for intensity-tunable metaholography working at visible frequencies

https://doi.org/10.1515/nanoph-2022-0075
Received February 14, 2022; accepted May 2, 2022;
published online May 16, 2022

Abstract: Tunable metasurfaces can replace conventional bulky active optical modules to realize practical flat optical devices such as lenses, LiDAR, holography, and augmented reality. However, tunable metasurfaces have generally been limited to switching between two distinct states. Here, we present liquid crystal (LC) integrated chiral metasurfaces, of which the metahologram intensity can be adjusted continuously between fully 'on' and 'off' states. The chiral metasurface consists of a gap-shifted split ring resonator (SRR), and exhibits spin angular momentum selection that reflects left-circularly-polarized light but perfectly absorbs right-circularly-polarized light (99.9%). The gap-shifted SRR realizes spin angular momentum selection using a metal–dielectric–metal multilayer structure and thereby induces a strong gap-plasmonic response, achieving the maximum calculated circular dichroism in reflection (CDR) of 0.99 at the wavelength of 635 nm. With the chiral metasurface, metaholograms are demonstrated with tunable intensities using LCs that change the polarization state of the output light using an applied voltage. With the LC integrated chiral metasurfaces, 23 steps of polarization are demonstrated for the continuous tuning of the holographic image intensity, achieving measured CDR of 0.91. The proposed LC integrated spin-selective chiral metasurface provides a new resource for development of compact active optical modules with continuously-tunable intensity.

Keywords: chiral plasmonics; chirality; metahologram; metasurface; tunable metasurface.

1 Introduction

Structured materials have been used to manipulate electromagnetic properties of light, such as amplitude, phase, polarization, and frequency [1–14]. Recently, metasurfaces composed of two-dimensional (2D) materials that have arrayed structures at a subwavelength scale have emerged as ultrathin flat optical components [15–24]. Structured materials can induce various optical responses that cannot be observed in nature depending on their periodicity, materials, and geometry of structures, therefore, the use of metasurfaces has been evaluated as a way to control light at will, including focusing light at the desired position [25–28], displaying high-resolution holographic images [29–36], miniaturizing sizes of high-brightness color pixels [37–39], tunable color display for sensing devices [40–42], and extreme beam-steering at desired angles with high efficiency [43]. Therefore, due to their compact form factor with subwavelength pixels, metasurfaces have the potential to be applied in augmented reality [44], LiDAR [45], photonic sensors [46, 47], dispersion controlling devices [48], selective light reflectors [49–52], absorbers [53–56], and microscopic components [57].

Younghwan Yang and Hongyoon Kim contributed equally to this work.

***Corresponding author: Junsuk Rho**, Department of Mechanical Engineering, Pohang University of Science and Technology (POSTECH), Pohang 37673, Republic of Korea; Department of Chemical Engineering, Pohang University of Science and Technology (POSTECH), Pohang 37673, Republic of Korea; POSCO-POSCTECH-RIST Convergence Research Center for Flat Optics and Metaphotonics, Pohang 37673, Republic of Korea; and National Institute of Nanomaterials Technology (NINT), Pohang 37673, Republic of Korea, E-mail: jsrho@postech.ac.kr. https://orcid.org/0000-0002-2179-2890

Younghwan Yang, Hongyoon Kim and Trevon Badloe, Department of Mechanical Engineering, Pohang University of Science and Technology (POSTECH), Pohang 37673, Republic of Korea, E-mail: younghwan@postech.ac.kr (Y. Yang), din1999dr@postech.ac.kr (H. Kim), trevon@postech.ac.kr (T. Badloe). https://orcid.org/0000-0003-2173-4217 (Y. Yang). https://orcid.org/0000-0003-2113-3921 (H. Kim). https://orcid.org/0000-0001-9458-6062 (T. Badloe)

Tunable metasurfaces have been widely explored with chemical, thermal, and mechanical stimuli due to the requirement of real-time active modulation of optical responses at visible frequencies [21, 58, 59]. Various tunable materials, including phase change materials (PCMs) and liquid crystals (LCs), have been proposed to actively manipulate scattering properties with those stimuli [58, 60]. However, previous tunable metasurfaces have been mainly exploited for the active modulation between two or a few more particular states. For example, PCM metasurfaces including vanadium dioxide (VO_2) [60–62], and germanium antimony tellurium alloy (GeSbTe, GST) [63, 64], controls the functionality of the metasurfaces using only two distinct states, neglecting the intermediate states. Additionally, in the case of LC integrated metasurfaces, even though the vectorial metaholography concept has been applied using LCs to increase the number of states, only LCP, RCP, and several elliptical polarization states is used, so the maximum number of reconstructed images is limited to nine [65]. Therefore, a method to fully utilize the elliptically polarized states between the RCP and LCP states of the tunable metasurface should be developed to increase the degree of freedom and for continuously tunable functionality.

Chiral metasurfaces are metasurfaces with structured materials that have mirror images that are not superimposable. Such metasurfaces can independently manipulate amplitude, phase, polarization, and frequencies of light depending on its spin angular momentum (SAM) [3, 5, 6]. Since independent control of different SAMs enables two selective scattering properties by manipulating spin states of input light, chiral metasurfaces have been actively investigated for tunable metasurfaces with polarization control of input light. Switchable images [66, 67], high-Q resonances [68], and nonreciprocal metaholograms [69] have been reported using chiral structured materials. However, previous chiral metasurfaces have been exploited only in the infrared regime [66, 67, 69], because strong chiral plasmonic responses require three-dimensional structures [3, 70], which cannot be fabricated using conventional methods that are compatible with complementary metal-oxide-semiconductor. Thus, the practical application of tunable chiral metasurfaces requires planar structured materials at visible wavelength scales with conventional fabrication methods.

Here, an electrically intensity tunable metahologram is designed by integrating an LC with spin-selective chiral metasurfaces. The combination undergoes a continuous change of holographic intensity in response to the applied voltage V_{ac} (Figure 1). The arrangement of the LC is controlled by V_{ac}, therefore enabling precise control of the polarization of the transmitted light. The transmitted light from the LC is left-circularly polarized (LCP) when V_{ac} = 1.18 V, and gradually becomes right-circularly polarized (RCP) as V_{ac} is increased from 1.18 to 1.39 V. The designed spin-selective chiral metasurface reflects incident LCP that creates images from an encoded computer-generated hologram, while perfectly absorbing the incident RCP. By exploiting the orthogonality of LCP and RCP, this LC-integrated spin-selective chiral metasurface can continuously control the intensity of a hologram by adjusting V_{ac} to change the proportion of incident LCP. Therefore, continuously intensity-tunable metaholography is achieved by controlling the voltage applied to the LC-assisted chiral metasurface.

2 Results and discussion

LC-integrated spin-selective chiral metasurfaces realize intensity-tunable metaholograms by adjusting V_{ac} (Figure 1A). Each LC functions as a quarter-wave plate with ordered molecules, and their optical axis is manipulated by changing the applied voltage. When 45° linearly-polarized light is incident to LCs, the output light can be changed to a desired polarization by adjusting V_{ac}. At V_{ac} = 1.39 V, the output polarization of LC is RCP, and the output polarization state is converted to LCP at V_{ac} = 1.18 V (Figure 1B). In addition, at 1.18 V ≤ V_{ac} ≤ 1.39 V, the output polarization is elliptically polarized light, i.e., a combination of LCP and RCP. Thus, depending on the proportion of LCP in the output light, the SAM-selective chiral metasurfaces produce holographic images with different intensities (Figure 1A–C). When V_{ac} = 1.39 V is applied to the LC, RCP is incident to the SAM selective chiral metasurface, and nearly all incident light (99.9%) is absorbed, so the metaholographic image has near-zero intensity (Figure 1C). In contrast, when V_{ac} = 1.18 V is applied to the LC, it transmits LCP, and the bright metaholographic images are reconstructed at the image plane (Figure 1C). The intensity of the holographic images can be continuously controlled by varying V_{ac} between 1.18 and 1.39 V. Various hologram intensities were experimentally achieved using 23 steps of polarization state (Figure 1C, Supplementary Material 1, Figure S1).

To achieve spin-selective chiral metasurfaces that perfectly absorb RCP at visible frequencies, gap-shifted split-ring resonators (SRR) are designed (Figure 2) using metal–dielectric–metal multilayer structures to produce strong gap-plasmonic responses [71] (Figure 2A(i)–C(i)). We simulate three SRRs with different gap displacements δ = 0, 30, and 60.5 nm, and with the same geometric parameter of length L = 345 nm of long axis, length S = 242 nm of short-axis, gap g = 58 nm, gold width w = 83 nm, gold thickness t_{Au} = 57 nm, SiO_2 thickness

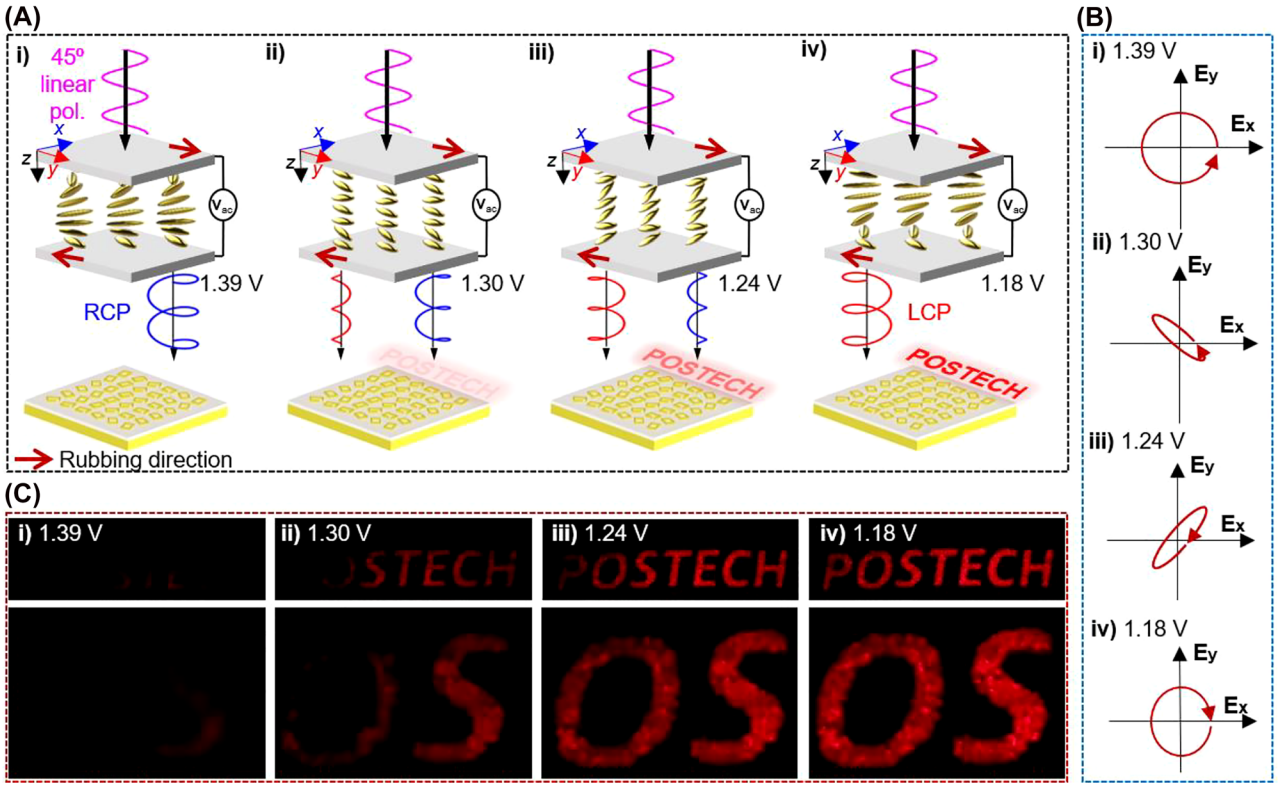

Figure 1: Schematic of electrically-tunable chiral metasurfaces for intensity manipulation of metaholography. (A) Schematic of electrically-tunable intensity of holograms with chiral metasurfaces. First, 45°-rotated linearly-polarized light is incident on the LC, and the polarization state of transmitted light is controlled by adjusting the applied voltage V_{ac}. As V_{ac} is decreased from 1.39 to 1.18 V, the transmitted RCP gradually decreases, while the transmitted LCP increases. The chiral metasurface only display the holographic image under LCP, so the reconstructed hologram intensity can be continuously tuned by adjusting V_{ac}. Red arrow: Rubbing direction. (B) Schematic of transmitted light polarization states from LC when V_{ac} was (i) 1.39 V, (ii) 1.30 V, (iii) 1.24 V, and (iv) 1.18 V. As V_{ac} decreased from 1.39 to 1.18 V, the polarization states changed from RCP to LCP. (C) Experimentally-obtained intensity-tunable holographic images when V_{ac} were (i) 1.39 V, (ii) 1.30 V, (iii) 1.24 V, and (iv) 1.18 V.

t_{SiO2} = 308 nm, and periodicity p = 450 nm. The SRR with δ = 0 shows a non-chiroptical response due to symmetry, and therefore has the same reflectance under both RCP and LCP incident light (Figure 2A(iii)). However, for the gap-shifted SRRs (δ = 30, 60.5 nm), the displacement of the gap positions breaks the mirror symmetry, therefore, chiroptical properties are observed in that the reflectance of RCP and LCP incident light differ (Figure 2B(iii) and C(iii)). The circular dichroism in reflection (CDR) is defined as the ratio of the normalized difference of the total reflectance of incident LCP and RCP: $(R_L - R_R)/(R_L + R_R)$, where R indicates reflectance, and the subscripts L and R represent the reflectance when LCP and RCP light is incident, respectively. The gap-shifted SRR with δ = 60.5 nm shows large inherent chiroptical characteristics, with a significant difference in reflectance under normal incident RCP and LCP illumination, achieving 99.9% absorption of RCP incidence, and 14.0% reflectance of LCP incident light at the wavelength λ = 635 nm (Figure 2C(iii)).

The CDR spectra for the three SRRs (δ = 0, 30, and 60.5 nm) are simulated with commercial finite element methods (Multiphysics, COMSOL v5.6) (Figure 3A). At δ = 60.5 nm, the gap shifted-SRR exhibit strong CDR (0.99) at the wavelength of 635 nm. The SRR with δ = 0 nm is achiral, and therefore has zero CDR over the entire spectrum due to the symmetry of the geometry, and the SRRs with δ = 30 nm exhibit maximum CDR at the wavelength of 706 nm, but it cannot be applied to SAM selective metasurfaces due to low CDR (details about CDR of gap-shifted SRR with δ = 30 nm see Supplementary Material 2, Figure S2). To analyze SAM conversion, the LCP and RCP components (R_{--}, R_{++}, R_{-+}, and R_{+-}) of reflectance are plotted in Figure 3B with subscripts + and – representing the LCP and RCP components, respectively; the former subscript indicates the output polarization states and the latter indicates the input. For example, R_{+-} denotes the reflectance component of the input RCP and output LCP. Thus, the total reflectance under RCP is the sum of R_{+-} and

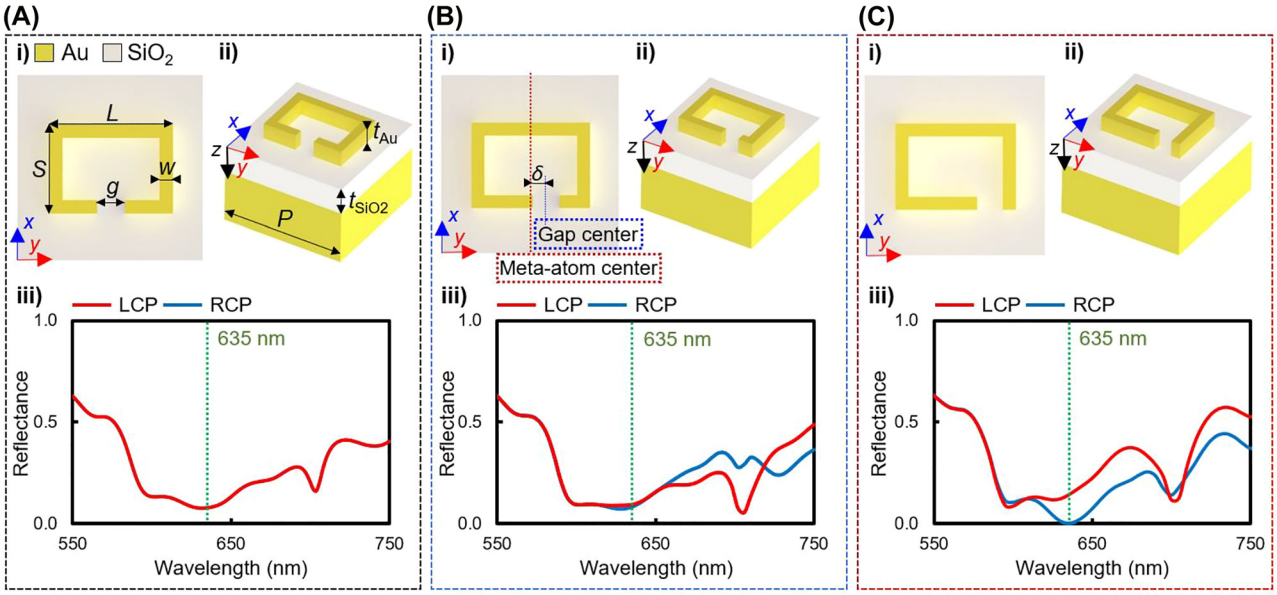

Figure 2: Effect of gap-shift on chiro-optical responses in split-ring resonators (SRR). Geometric parameters of the gap-shifted SRRs are long-axis length L, short-axis length S, gap g, gold width w, Au thickness t_{Au}, and SiO_2 thickness t_{SiO2}, gap displacement δ, and periodicity P. Geometric parameters are $L = 345$ nm, $S = 242$ nm, $g = 58$ nm, $w = 83$ nm, $t_{Au} = 57$ nm, $t_{SiO2} = 308$ nm, and $p = 450$ nm. Simulated reflectance spectra of three SRRs, that have gaps in (A(i)) The center ($\delta = 0$ nm) (B(i)) The mid-right ($\delta = 30$ nm), and (C(i)) The right ($\delta = 60.5$ nm). Red dotted line: center of unit cell; blue dotted line: center of gap. (i) Top-view, (ii) tilted view of unit cells, and (iii) simulated reflectance under LCP and RCP, respectively.

R_{++}. For the gap-shifted SRR with $\delta = 60.5$ nm, $R_{-+} = 0.140$ at $\lambda = 635$ nm and the other reflectance are near zero ($R_{+-} = 5.90 \times 10^{-4}$, $R_{++} = 5.13 \times 10^{-5}$, $R_{--} = 5.34 \times 10^{-5}$), so RCP incident light is perfectly absorbed and only LCP incident light is reflected and converted to RCP light.

The impedance-matching conditions are further investigated to reveal the mechanism of perfect absorption in the gap-shifted SRR with $\delta = 60.5$ nm. Assuming that the structure is homogeneous, the effective impedance z of an SRR is calculated using the S-parameter retrieval method [72]:

$$z = \pm\sqrt{\frac{(1+S_{11})^2 - S_{21}^2}{(1-S_{11})^2 - S_{21}^2}}, \quad (1)$$

where S is the S-parameter element; and the former and latter subscripts represent the output and input components, respectively. When the impedance of the metasurface matches the air impedance, which is 1, the metasurface functions as a perfect absorber. The impedance of the gap-shifted SRR ($\delta = 60.5$ nm) is calculated for RCP incidence (Figure 3C), where at $\lambda = 635$ nm, the real part of the impedance is 1.01, and the imaginary part is 0.0321, which are similar to the impedance of the air and there, yield perfect absorption. On the other hand, the effective impedance of $z = 0.451 - 0.0190i$ under LCP incidence at $\lambda = 635$ nm does not match that of air, so perfect absorption is not achieved due to the impedance mismatch (Supplementary Material 3, Figure S2). In addition, the gap-shifted SRR ($\delta = 60.5$ nm) showed robustness in incident angle. The CDR maintains >0.95 where an incident angle θ_x and θ_y are under 7° and 6°, respectively. After that, they continuously decrease as the incident angle θ_x and θ_y increase to 50° (Figure 3D, details in Supplementary Materials 4).

For the spin-selective metahologram that works at $\lambda = 635$ nm, the concept of reflective geometric metasurfaces [73] is used to demonstrate metaholography by using the gap-shifted SRR ($\delta = 60.5$ nm) as a unit cell, because the SRR completely absorbs RCP and converts 14.0% of LCP to RCP, which is essential for the use of Pancharatnam–Berry (PB) phase, as PB phase utilizes conversion efficiency to modulate the phase. To reconstruct the holographic images, the phase distribution of the hologram is retrieved using the iterative Gerchberg–Saxton (GS) algorithm (details in Supplementary Material 5). The phase of each pixel is encoded using the geometric PB phase, which achieves phase 2θ by rotating the nanostructure unit cells by an angle θ, and was designed to exhibit off-axis images to avoid overlapping with zeroth-order diffraction. By rotating the gap-shifted SRR ($\delta = 60.5$ nm), from 0 to 180° in the xy-plane, 0 to 2π phase is achieved by the PB phase as shown in Figure 4A. The phase retardation is almost proportional to the rotation angle of the SRR, and small variations may be a

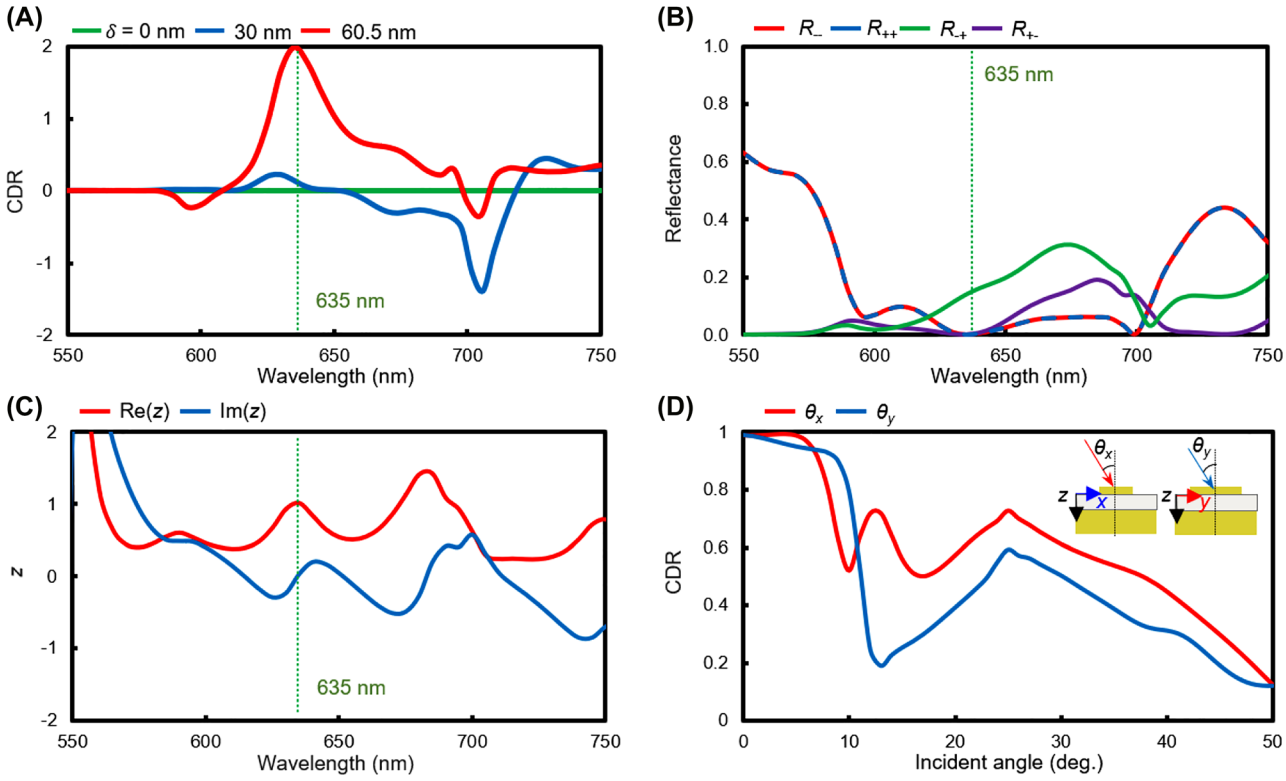

Figure 3: Chiroptical responses of the gap-shifted SRR. (A) Calculated circular dichroism in reflection (CDR) when the gap displacement δ is varied as 0, 30, and 60.5 nm. (B) Reflectance components of the gap-shifted SRR (δ = 60.5 nm). (C) Calculated effective impedance z of the gap-shifted SRR (δ = 60.5 nm) under RCP incidence. The dotted green line indicates the wavelength of 635 nm, where the metasurfaces perfectly absorb incident RCP. (D) Calculated CDR of the gap-shifted SRR (δ = 60.5 nm) depending on the incident angle from 0 to 50°. θ_x and θ_y denote incident angles with respect to the *yz*- and *xz*-plane, respectively.

result of interaction between adjacent SRRs. Reflected electric-field profiles are calculated when the SRR is rotated in eight steps between 0 and 180°; the profiles shift in proportion to the rotation (Figure 4B).

As a proof-of-concept of the spin-selective metahologram, holographic images are measured using a home-made optical setup that is composed of a compact diode 635 nm laser, linear polarizer (LP), quarter-wave plates (QWP), and pinhole with a diameter of 300 μm (Figure 4C). LCP and RCP are created by placing the LP and the QWP on the optical paths. The light is incident on the fabricated reflective spin-selective metasurface composed of rotated gap-shifted SRR (δ = 60.5 nm) unit cells that are rotated to encode the desired phase at each spatial location, and the screen was placed off-axis at the same side of the beam to avoid the zeroth-order beam. Figure 4D shows an SEM image of part of the fabricated spin-selective metasurface. Using the experimental setup in Figure 4C, a clear holographic image of the word 'POSTECH' is observed on the image plane when illuminated by LCP (Figure 4E(i)); however, the image disappears under RCP incidence and also with the zeroth-order diffracted light, because the metasurface completely absorbs RCP (Figure 4E(ii)). This result demonstrates the spin-selective characteristics of the metasurface.

To realize a continuously-tunable intensity of hologram, the gap-shifted SRRs were integrated with LCs, which act as a retarder and function as an electrically-tunable QWP (Figure 5A). The LCs, 4-cyano-4′pentylbiphenyl (5CB); their refractive index (extraordinary refractive index n_e) on the long axis differs from that on the short axis (ordinary refractive index n_o). The effective refractive index of the LC cells n_{eff} is defined as $n_o n_e / \sqrt{n_o^2 \cos^2(\alpha) + n_e^2 \cos^2(\alpha)} - n_o$, where α is the angle between the rubbing direction and the long axis [74, 75]. The LCs reorder their long axis to be parallel to the direction of an applied electrical field, varying their optical axis in response to V_{ac}, allowing them to act as phase retarders. The amount of the phase retardation is defined as $\tau = \int_0^t 2\pi \Delta n_{eff}(z)/\lambda dz$ rad, where t is the thickness of the LC cell [74, 75]. Consequently, by combining the LC with the 45°-rotated LP, the output light can be controlled from LCP to RCP by precisely manipulating V_{ac}. The possible

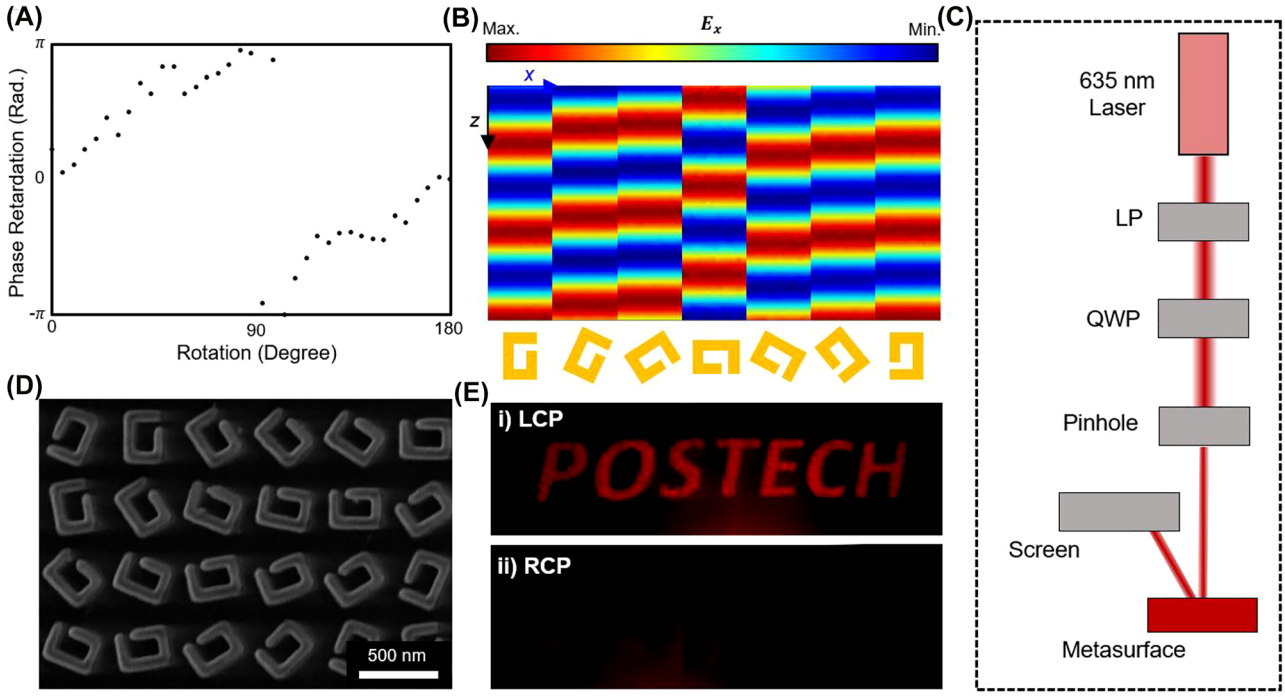

Figure 4: Demonstration of the spin-selective chiral metasurface. (A) Simulation of phase retardation depending on the rotation angle of the gap-shifted SRR under LCP. When LCP is incident to the metasurface, the phase of output light is retarded proportional to the rotation angle of gap-shifted SRRs. (B) Normalized electrical field $\boldsymbol{E}_x$ of the reflected light from rotated gap-shifted SRR that shows the PB phase of the chiral nanostructure under incident LCP. (C) Optical setup designed with 635 nm laser, linear polarizer (LP), quarter-wave plate (QWP), and 300 μm diameter pinhole for the proof of concept of the spin-selective metahologram. Holographic metasurface was designed as an off-axis hologram to avoid overlapping of zeroth-order diffraction light and hologram image. (D) Top view scanning electron microscope image of the fabricated metasurface. (E) Holographic image 'POSTECH' is obtained under (i) incident LCP, and disappears under (ii) RCP. Twin images are not obtained under both RCP and LCP, which are omitted from the figure for clarity.

polarization states of output light can be represented using a Poincaré sphere (Figure 5B). The polarization is rotated with respect to the S1 axis of the Poincaré sphere when the input light is 45°-rotated linearly polarized light (Figure 5B, green square). A detailed description of LC for implanting in metasurfaces is given in refs. [65, 76].

For the case when 45°-rotated linearly polarized light (green square in S2–S3 plane on the Poincaré sphere) is incident to the LC, when V_{ac} = 0 V, the LC had τ = 18.3 rad, which is 2.9 turns on the S2–S3 plane in Poincaré sphere with respect to the S1 axis (Figure 5B, black dot). When V_{ac} is applied to the LC, the τ of the LC decreases, and the polarization states that pass through the LC rotates clockwise on the S2–S3 plane in the Poincaré sphere with respect to the S1 axis (Figure 5B) [65]. Here, the S1 axis corresponds to the rubbing direction. By continuously increasing V_{ac}, we determined that V_{ac} = 1.39 V results in RCP (blue square) output polarization, and V_{ac} = 1.18 V results in LCP (red square) output polarization, respectively. V_{ac} between these RCP and LCP values creates elliptical polarization states that are composed of RCP and LCP, and when V_{ac} increases and get closer to 1.39 V, the LCP ratio decreases so the intensity of the hologram decreases.

The intensity of the reconstructed hologram image was measured, and it is consistent with the simulated conversion efficiency of the gap-shifted SRR (Figure 5C). The simulation was conducted by changing the input polarization states to the spin-selective metasurface that corresponds to applied V_{ac}; the contrast of reconstructed hologram intensity reaches ~1:240, which agrees with the calculated conversion efficiency (14.0% for LCP incidence, 0.0590% for RCP incidence). The reconstructed hologram intensity is measured as 0.022 μW at V_{ac} = 1.18 V and 0.001 μW at V_{ac} = 1.39 V, which is 22 times larger, reaching CDR of 0.91 (details in Section 4). The discrepancy between simulated and measured intensity originates from (1) minor thickness variation in homemade LC cells, and (2) fabrication defects in realized metasurfaces. These discrepancies can be corrected through optimization of the LC-made and the metasurface manufacturing process. As a

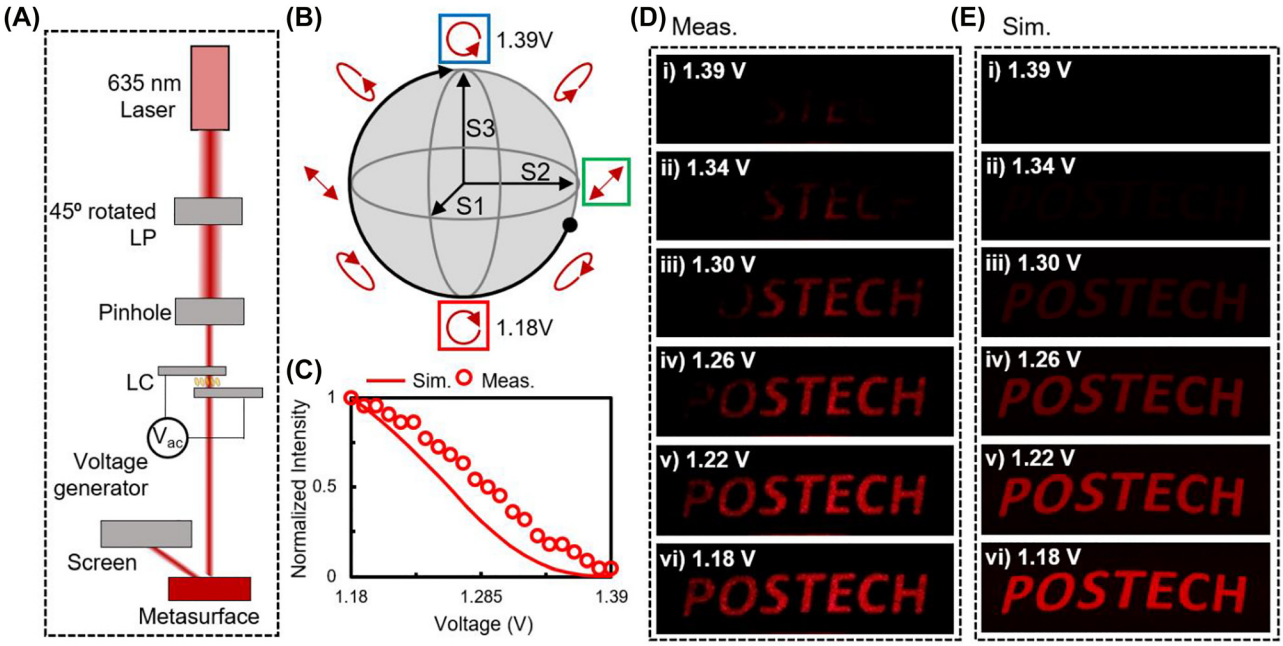

Figure 5: Demonstration of electrically-tunable intensity using LC-assisted spin-selective chiral metasurfaces. (A) Schematic of the optical setup for electrically-tunable intensity with LC-assisted spin-selective chiral metasurfaces. (B) Output polarization states pass through the LC when 45° rotated linearly polarized light is incident. Green, red, and blue squares: Incident and output polarization states when V_{ac} is 1.18 and 1.39 V, respectively. Black dot: polarization states at V_{ac} = 0 V (C) Calculated (solid line) and measured (dotted line) intensity of metaholograms. (D) Measured and (E) simulated continuous intensity-tunable holograms when V_{ac} were (i) 1.39 V, (ii) 1.34 V, (iii) 1.30 V, (iv) 1.26 V, (v) 1.22 V, and (vi) 1.18 V.

result, by continuously modulating V_{ac} (in the experiment, increments of 0.01 V) from 1.39 to 1.18 V, the intensity of the holographic image 'POSTECH' is continuously increased (Figures 5D and S3). We assume that the incident light has uniform light intensity distribution (not the Gaussian beam) because the beam size is enough to fully cover that of metasurfaces.

To verify the intensity-tunable metahologram, measured holographic images are compared with simulated reconstructed holographic images depending on applied V_{ac} from 1.39 to 1.18 V (Figure 5E). In the measured reconstructed holograms, the center characters of the word 'ST' exhibit higher intensity than that of the side ones. However, simulated reconstructed holograms have coherent intensity tunability regardless of the position of the characters. The different intensity may be induced by different distances from the reflective metasurface to the point of the reconstructed image on the screen. Side characters have more distance than center characters, so they are turned off more rapidly. This discrepancy can be further corrected by modifying the intensity of the initial target images.

3 Conclusions

In conclusion, we designed spin-selective chiral metasurfaces composed of the gap-shifted SRR and implanted them with LC cells to achieve electrically intensity-tunable metaholography. The measured CDR of our device approaches 0.91, and its theoretical value reaches 0.99 at λ = 635 nm, enabling perfect SAM selection by the gap-shifted SRR. The measured CDR of 0.91 is the highest value of any previously reported PB-phase based chiral plasmonic metasurfaces working at the visible and infrared regions (Table 1). In addition, the SAM selective chiral metasurfaces can be fabricated using conventional electron-beam lithography and deposition processes, so it has higher fabrication feasibility than previously-reported three-dimensional chiral plasmonic metasurfaces such as helical structures [66] (Table 1).

Compared to dielectric metasurfaces that exploit the PB phase, the SAM selective chiral metasurface has the advantage that the output phase map is not reversed when the input handedness is converted. When input light has

Table 1: Comparison of chiral structural materials for PB-phase metasurfaces working at the near-infrared and visible frequencies. All CDR value is calculated as an absolute value of $(R_R - R_L)/(R_R + R_L)$ for clear comparison. For transmissive metasurfaces, CDRs are replaced by circular dichroism on transmission (CDT) that is expressed as an absolute value of $(T_R - T_L)/(T_R + T_L)$. Superscripts: CDR, CDT calculated by (a): simulation, (b): measurement.

Year [Reference]	Wavelength (nm)	CDR, CDT	Materials	Fabrication feasibility (Geometric dimension)	Usage
Our work	635	0.99[a], 0.91[b]	Au, SiO_2	High (2D)	Hologram
2017 [79]	1,560	0.99[a], 0.78[b]	Si	High (2D)	Wave plate
2018 [80]	1,655	0.86[a]	Ge	High (2D)	Hologram
2018 [66]	806	0.91[a], 0.77[b]	Au	Low (3D)	Hologram
2020 [81]	792	0.30[a]	Lithium niobate	High (2D)	–
2020 [82]	633	0.43[a], 0.45[b]	a-Si:H	High (2D)	Hologram
2020 [83]	1,384[a], 1,400[b]	0.99[a], 0.88[b]	Al, SiO_2	High (2D)	Color printing
2021 [34]	633	0.82[a], 0.84[b]	a-Si:H	High (2D)	–

imperfect circular polarization states such as elliptical or linear polarization, the conventional dielectric metasurface for metaholograms and metalenses cannot avoid twin-holographic images and dispersion of light, respectively. Although combining the geometrical phase with the propagation phase has been evaluated as a way to generate independent responses depending on the handedness of input circularly polarized light [77, 78], their structured materials have low fabrication tolerance, because they require both desired amplitude and phase profiles. Thus, the SAM selective metasurfaces can be beneficial to avoid noise (e.g., twin hologram images) caused by imperfectly polarized light when metalenses and metaholograms are designed.

Although previous research commented that plasmonic structures have the limitation on their unavoidable intrinsic losses and that high index dielectrics (e.g. titanium dioxide, silicon nitride, etc.) will be the dominant material, we believe that their optical losses can be used in a practical way (herein, perfect absorption of certain circularly polarized light), opening new application fields of plasmonic metasurfaces. Considering that LC cells can be closely packed by locating them directly on the metasurfaces to make a more compact form factor [65, 76], we believe that the SAM selective chiral metasurface will become one more option for photonic devices that work at visible frequencies.

4 Experimental section

4.1 Numerical simulations

Numerical simulations were conducted using the commercially available finite element method (FEM) solver, COMSOL Multiphysics v5.6. Simulations of reflectance coefficient, impedance, phases, and reflected intensity profiles were calculated using periodic boundary conditions in the x and y directions, and perfect boundary conditions in the z-direction.

4.2 Fabrication of metasurfaces

The designed metasurfaces were fabricated using conventional manufacturing methods, including electron-beam lithography and electron beam deposition. Firstly, a 300 nm-thick gold (Au) and 308 nm-thick silicon dioxide (SiO_2) layer were sequentially deposited on a silicon (Si) wafer using electron beam deposition. Electron-beam resists (Microchem, PMMA 495 A6) were spin-coated on the sample at 2000 rpm for 1 min, then baked at 180 °C for 5 min. The resist was exposed to electron-beam following prepared nanopatterns at 100 kV using electron-beam lithography (Elionix, ELS-7000). And then, the sample was immersed in a developer (Microchem, MIBK: IPA = 1:3) at 0 °C for 10 min to remove exposed patterns. Electron beam deposition was used to deposit a 57 nm-thick Au film on the sample, and it was immersed in acetone at 60 °C for 12 h to lift off the unexposed area to complete the sample fabrication.

4.3 Fabrication of LC cells

The LC cells were prepared using polyimides (Nissan Chemical Korea) for the alignment layer, and indium tin oxide (ITO) coated glass plates. The polyimides were spin-coated, baked, and rubbed to create a rubbing direction for unidirectional alignment for LCs. Two substrates were prepared using the same method as in Section 4.2. After assembling two substrates with a gap of 10 μm by using UV-glue (Norland Products Inc., NOA 65) and glass spacer, sandwiched cells were filled with nematic LCs (Jiangsu Hucheng Display Technology Co., Ltd). Specific methods are detained in refs. [65, 76].

Author contributions: J.R., Y.Y., and H.K. conceived the idea and initiated the work. Y.Y designed LC-integrated gap-shifted SRR, and H.K. optimized the geometrical parameters of the structural materials. H.K. analyzed the

absorption mechanism of gap-shifted SRRs using numerical simulations. Y.Y. fabricated the gap-shifted SRR metasurfaces and integrated the LC. Y.Y and H.K. captured the holographic images with voltage generator and home-made setup. Y.Y. and H.K. mainly wrote the manuscript, and T.B. partially involved. J.R. guided the entire project. All the authors have accepted the final manuscript and approved the submission.

Research funding: This work was financially supported by the POSCO-POSTECH-RIST Convergence Research Center program funded by POSCO, the LGD-SNU incubation program funded by LG Display, and the National Research Foundation (NRF) grants (NRF-2021M3H4A1A04086554, CAMM-2019M3A6B3030637). Y.Y. acknowledges the Hyundai Motor *Chung Mong-Koo* fellowship, and the NRF fellowship (NRF-2021R1A6A3A13038935) funded by the Ministry of Education, Republic of Korea. H.K. acknowledges POSTECH Alchemist fellowship.

Conflict of interest statement: The authors declare no conflicts of interest regarding this article.

References

[1] M. Kadic, G. W. Milton, M. V. Hecke, and M. Wegener, "3D metamaterials," *Nat. Rev. Phys.*, vol. 1, pp. 198–210, 2019.

[2] S. Jahani and Z. Jacob, "All-dielectric metamaterials," *Nat. Nanotechnol.*, vol. 11, pp. 23–36, 2016.

[3] J. Mun, M. Kim, Y. Yang, et al., "Electromagnetic chirality: from fundamentals to nontraditional chiroptical phenomena," *Light Sci. Appl.*, vol. 9, p. 139, 2020.

[4] N. Meinzer, W. L. Barnes, and R. Hooper, "Plasmonic meta-atoms and metasurfaces," *Nat. Photon.*, vol. 8, pp. 889–898, 2014.

[5] Y. Kim, H. Kim, Y. Yang, T. Badloe, N. Jeon, and J. Rho, "Three-dimensional artificial chirality towards low-cost and ultra-sensitive enantioselective sensing," *Nanoscale*, vol. 14, pp. 3720–3730, 2021.

[6] Y. Yang, Y. Kim, J. Gwak, et al., "Realization of artificial chirality in micro-/nano-scale three-dimensional plasmonic structures," in *Chirality, Magnetism and Magnetoelectricity*, Cham, Springer, vol. 138, pp. 241–263, 2021.

[7] J. Kim, Y. Yang, T. Badloe, I. Kim, G. Yoon, and J. Rho, "Geometric and physical configurations of meta-atoms for advanced metasurface holography," *InfoMat*, vol. 3, pp. 739–754, 2021.

[8] D. Lee, S. So, G. Hu, et al., "Hyperbolic metamaterials: fusing artificial structures to natural 2D materials," *eLight*, vol. 2, p. 1, 2022.

[9] D. Lee, M. Kim, and J. Rho, "Next-generation imaging techniques: functional and miniaturized optical lenses based on metamaterials and metasurfaces," *Micromachines*, vol. 12, p. 1142, 2021.

[10] Y. Zhang, H. Liu, H. Cheng, J. Tian, and S. Chen, "Multidimensional manipulation of wave fields based on artificial microstructures," *Opto-Electron. Adv.*, vol. 3, p. 200002, 2020.

[11] J. Kim, J. Seong, Y. Yang, S.-W. Moon, T. Badloe, and J. Rho, "Tunable metasurfaces towards versatile metalenses and metaholograms: a review," *Adv. Photonics*, vol. 4, p. 024001, 2022.

[12] J. Kim, D. Jeon, J. Seong, et al., "Photonic encryption platform via dual-band vectorial metaholograms in the ultraviolet and visible," *ACS Nano*, vol. 16, pp. 3546–3553, 2022.

[13] S.-W. Moon, C. Lee, Y. Yang, et al., "Tutorial on metalenses for advanced flat optics: design, fabrication, and critical considerations," *J. Appl. Phys.*, vol. 131, p. 091101, 2022.

[14] J. Noh, Y. H. Nam, S. So, et al., "Design of a transmissive metasurface antenna using deep neural networks," *Opt. Mater. Express*, vol. 11, pp. 2310–2317, 2021.

[15] G. Li, S. Zhang, and T. Zentgraf, "Nonlinear photonic metasurfaces," *Nat. Rev. Mater.*, vol. 2, p. 17010, 2017.

[16] A. S. Solntsev, G. S. Agarwal, and Y. S. Kivshar, "Metasurfaces for quantum photonics," *Nat. Photon.*, vol. 15, pp. 327–336, 2021.

[17] W. T. Chen, A. Y. Zhu, and F. Capasso, "Flat optics with dispersion-engineered metasurfaces," *Nat. Rev. Mater.*, vol. 5, pp. 604–620, 2020.

[18] S.-W. Moon, Y. Kim, G. Yoon, and J. Rho, "Recent progress on ultrathin metalenses for flat optics," *iScience*, vol. 23, p. 101877, 2020.

[19] G. Yoon, T. Tanaka, T. Zentgraf, and J. Rho, "Recent progress on metasurfaces: applications and fabrication," *J. Phys. D Appl. Phys.*, vol. 54, p. 383002, 2021.

[20] H. Jeong, Y. Yang, H. Cho, et al., "Emerging advanced metasurfaces: alternatives to conventional bulk optical devices," *Microelectron. Eng.*, vol. 220, p. 111146, 2020.

[21] H. Ahmed, H. Kim, Y. Zhang, et al., "Optical metasurfaces for generating and manipulating optical vortex beams," *Nanophotonics*, vol. 11, pp. 941–956, 2022.

[22] H. Ren, X. Fang, J. Jang, J. Bürger, J. Rho, and S. A. Maier, "Complex-amplitude metasurface-based orbital angular momentum holography in momentum space," *Nat. Nanotechnol.*, vol. 15, pp. 948–955, 2020.

[23] G. Kim, S. Kim, H. Kim, J. Lee, T. Badloe, and J. Rho, "Metasurface-empowered spectral and spatial light modulation for disruptive holographic displays," *Nanoscale*, vol. 14, pp. 4380–4410, 2022.

[24] C. Jung, S.-J. Kim, J. Jang, et al., "Disordered-nanoparticle–based etalon for ultrafast humidity-responsive colorimetric sensors and anti-counterfeiting displays," *Sci. Adv.*, vol. 8, p. eabm8598, 2022.

[25] G. Yoon, K. Kim, D. Huh, H. Lee, and J. Rho, "Single-step manufacturing of hierarchical dielectric metalens in the visible," *Nat. Commun.*, vol. 11, p. 2268, 2020.

[26] H. Cho, H. Jeong, Y. Yang, T. Badloe, and J. Rho, "Enhancement of luminous intensity emission from incoherent LED light sources within the detection angle of 10° using metalenses," *Nanomaterials*, vol. 12, p. 153, 2022.

[27] K. Kim, G. Yoon, S. Baek, J. Rho, and H. Lee, "Facile nanocasting of dielectric metasurfaces with sub-100 nm resolution," *ACS Appl. Mater. Interfaces*, vol. 11, pp. 26109–26115, 2019.

[28] G. Yoon, K. Kim, S.-U. Kim, S. Han, H. Lee, and J. Rho, "Printable nanocomposite metalens for high-contrast near-infrared imaging," *ACS Nano*, vol. 15, pp. 698–706, 2021.

[29] M. A. Ansari, I. Kim, D. Lee, et al., "A spin-encoded all-dielectric metahologram for visible light," *Laser Photonics Rev.*, vol. 13, p. 1900065, 2019.
[30] G. Yoon, D. Lee, K. T. Nam, and J. Rho, "Pragmatic metasurface hologram at visible wavelength: the balance between diffraction efficiency and fabrication compatibility," *ACS Photonics*, vol. 5, pp. 1643–1647, 2018.
[31] Z. Li, I. Kim, L. Zhang, et al., "Dielectric meta-holograms enabled with dual magnetic resonances in visible light," *ACS Nano*, vol. 11, pp. 9382–9389, 2017.
[32] M. A. Ansari, I. Kim, I. D. Rukhlenko, et al., "Engineering spin and antiferromagnetic resonances to realize an efficient direction-multiplexed visible meta-hologram," *Nanoscale Horiz*, vol. 5, pp. 57–64, 2019.
[33] I. Kim, H. Jeong, J. Kim, et al., "Dual-band operating metaholograms with heterogeneous meta-atoms in the visible and near-infrared," *Adv. Opt. Mater.*, vol. 9, p. 2100609, 2021.
[34] H. S. Khaliq, I. Kim, A. Zahid, et al., "Giant chiro-optical responses in multipolar-resonances-based single-layer dielectric metasurfaces," *Photonics Res.*, vol. 9, pp. 1667–1674, 2021.
[35] Z.-L. Deng, M. Jin, X. Ye, et al., "Full-color complex-amplitude vectorial holograms based on multi-freedom metasurfaces," *Adv. Funct. Mater.*, vol. 30, p. 1910610, 2020.
[36] J. Kim, D. K. Oh, H. Kim, et al., "Metasurface holography over 90% efficiency in the visible via nanoparticle-embedded-resin printing," arXiv.2109.01141, 2021.
[37] J. Jang, T. Badloe, Y. Yang, T. Lee, J. Mun, and J. Rho, "Spectral modulation through the hybridization of Mie-scatterers and quasi-guided mode resonances: realizing full and gradients of structural color," *ACS Nano*, vol. 14, pp. 15317–15326, 2020.
[38] C. Jung, Y. Yang, J. Jang, et al., "Near-zero reflection of all-dielectric structural coloration enabling polarization-sensitive optical encryption with enhanced switchability," *Nanophotonics*, vol. 10, pp. 919–926, 2021.
[39] T. Lee, J. Kim, I. Koirala, et al., "Nearly perfect transmissive subtractive coloration through the spectral amplification of Mie scattering and lattice resonance," *ACS Appl. Mater. Interfaces*, vol. 13, pp. 26299–26307, 2021.
[40] Y. J. Yoo, W. G. Kim, J. H. Ko, et al., "Large-area virus coated ultrathin colormetric sensors with a highly lossy resonant promoter for enhanced chromaticity," *Adv. Sci.*, vol. 7, p. 2000978, 2020.
[41] Y. J. Kim, Y. J. Yoo, M. H. Kang, et al., "Mechanotunable optical filters based on stretchable silicon nanowire arrays," *Nanophotonics*, vol. 9, pp. 3287–3293, 2020.
[42] J. H. Ko, Y. J. Yoo, Y. J. Kim, S.-S. Lee, and Y. M. Song, "Flexible, large-area covert polarization display based on ultrathin lossy nanocolumns on a metal film," *Adv. Funct. Mater.*, vol. 30, p. 1908592, 2020.
[43] Y. Yang, G. Yoon, S. Park, et al., "Revealing structural disorder in hydrogenated amorphous silicon for a low-loss photonic platform at visible frequencies," *Adv. Mater.*, vol. 33, p. 2005893, 2021.
[44] J. Xiong, E.-L. Hsiang, Z. He, T. Zhan, and S.-T. Wu, "Augmented reality and virtual reality displays: emerging technologies and future perspectives," *Light Sci. Appl.*, vol. 10, p. 216, 2021.
[45] I. Kim, R. J. Martins, J. Jang, et al., "Nanophotonics for light detection and ranging technology," *Nat. Nanotechnol.*, vol. 16, pp. 508–524, 2021.
[46] Y. Yang, T. Lee, M. Kim, et al., "Dynamic optical spin Hall effect in chitosan-coated all-dielectric metamaterials for a biosensing platform," *IEEE J. Sel.Top. Quantum Electron.*, vol. 27, p. 7300608, 2021.
[47] I. Kim, W.-S. Kim, K. Kim, et al., "Holographic metasurface gas sensors for instantaneous visual alarms," *Sci. Adv.*, vol. 7, p. eabe9943, 2021.
[48] K. Dou, X. Xie, M. Pu, et al., "Off-axis multi-wavelength dispersion controlling metalens for multi-color imaging," *Opto-Electron. Adv.*, vol. 3, p. 190005–190007, 2020.
[49] M. Kim, D. Lee, Y. Yang, and J. Rho, "Switchable diurnal radiative cooling by doped VO_2," *Opto-Electron. Adv*, vol. 4, p. 200006, 2021.
[50] M. Kim, D. Lee, S. Son, Y. Yang, H. Lee, and J. Rho, "Visibly transparent radiative cooler under direct sunlight," *Adv. Opt. Mater.*, vol. 9, p. 2002226, 2021.
[51] S. So, Y. Yang, S. Son, et al., "Highly suppressed solar absorption in a daytime radiative cooler designed by genetic algorithm," *Nanophotonics*, vol. 11, pp. 2107–2115, 2021.
[52] Y. Lu, Y. Xu, X. Ouyang, et al., "Cylindrical vector beams reveal radiationless anapole condition in a resonant state," *Opto-Electron. Adv.*, vol. 7, p. 210014, 2022.
[53] S. So, Y. Yang, T. Lee, and J. Rho, "On-demand design of spectrally sensitive multiband absorbers using an artificial neural network," *Photonics Res*, vol. 9, pp. B153–B158, 2021.
[54] T. Badloe, J. Mun, and J. Rho, "Metasurfaces-based absorption and reflection control: perfect absorbers and reflectors," *J. Nanomater.*, vol. 2017, p. e2361042, 2017.
[55] T. Badloe, I. Kim, Y. Kim, J. Kim, and J. Rho, "Electrically tunable bifocal metalens with diffraction-limited focusing and imaging at visible wavelengths," *Adv. Sci.*, vol. 8, p. 2102646, 2021.
[56] D. Lee, M. Go, M. Kim, et al., "Multiple-patterning colloidal lithography-implemented scalable manufacturing of heat-tolerant titanium nitride broadband absorbers in the visible to near-infrared," *Microsyst. Nanoeng.*, vol. 7, p. 14, 2021.
[57] D. Lee, Y. Yang, G. Yoon, M. Kim, and J. Rho, "Resolution enhancement of fluorescence microscopy using encoded patterns from all-dielectric metasurfaces," *Appl. Phys. Lett.*, vol. 115, p. 101102, 2019.
[58] T. Badloe, J. Lee, J. Seong, and J. Rho, "Tunable metasurfaces: the path to fully active nanophotonics," *Adv. Photonics Res.*, vol. 2, p. 2000205, 2021.
[59] S. Park, C. Park, Y. J. Hwang, et al., "Focus-tunable planar lenses by controlled carriers over exciton," *Adv. Opt. Mater.*, vol. 9, p. 2001526, 2021.
[60] B. Ko, T. Badloe, and J. Rho, "Vanadium dioxide for dynamically tunable photonics," *ChemNanoMat*, vol. 7, pp. 713–727, 2021.
[61] B. Ko, J. Y. Chae, T. Badloe, et al., "Multilevel absorbers via the integration of undoped and tungsten-doped multilayered vanadium dioxide thin films," *ACS Appl. Mater. Interfaces*, vol. 14, pp. 1404–1412, 2022.
[62] B. Ko, T. Badloe, S.-J. Kim, S.-H. Hong, and J. Rho, "Employing vanadium dioxide nanoparticles for flexible metasurfaces with switchable absorption properties at near-infrared frequencies," *J. Opt.*, vol. 22, p. 114002, 2020.
[63] Y. Chen, X. Duan, M. Matuschek, et al., "Dynamic color displays using stepwise cavity resonators," *Nano Lett.*, vol. 17, pp. 5555–5560, 2017.
[64] F. Sterl, N. Strohfeldt, R. Walter, R. Griessen, A. Tittl, and H. Giessen, "Magnesium as novel material for active plasmonics in the visible wavelength range," *Nano Lett.*, vol. 15, pp. 7949–7955, 2015.

[65] I. Kim, J. Jang, G. Kim, et al., "Pixelated bifunctional metasurface-driven dynamic vectorial holographic color prints for photonic security platform," *Nat. Commun.*, vol. 12, p. 3614, 2021.
[66] Y. Chen, X. Yang, and J. Gao, "Spin-controlled wavefront shaping with plasmonic chiral geometric metasurfaces," *Light Sci. Appl.*, vol. 7, p. 84, 2018.
[67] Q. Wang, Q. Yang, X. Zhang, et al., "Reflective chiral meta-holography: multiplexing holograms for circularly polarized waves," *Light Sci. Appl.*, vol. 7, p. 25, 2018.
[68] T. Shi, Z. L. Deng, G. Geng, et al., "Planar chiral metasurfaces with maximal tunable chiroptical response driven by bound states in the continuum," arXiv:2112.07122, 2022.
[69] K. Chen, G. Ding, G. Hu, et al., "Directional janus metasurface," *Adv. Mater.*, vol. 32, p. 1906352, 2020.
[70] Z. Liu, H. Du, J. Li, L. Lu, Z.-Y. Li, and N. X. Fang, "Nano-kirigami with giant optical chirality," *Sci. Adv.*, vol. 4, p. eaat4436, 2018.
[71] C. Jung, G. Kim, M. Jeong, et al., "Metasurface-driven optically variable devices," *Chem. Rev.*, vol. 121, pp. 13013–13050, 2021.
[72] D. R. Smith, D. C. Vier, Th. Koschny, and C. M. Soukoulis, "Electromagnetic parameter retrieval from inhomogeneous metamaterials," *Phys. Rev. E*, vol. 71, p. 036617, 2005.
[73] G. Zheng, H. Mühlenbernd, M. Kenney, G. Li, T. Zentgraf, and S. Zhang, "Metasurface holograms reaching 80% efficiency," *Nat. Nanotechnol.*, vol. 10, pp. 308–312, 2015.
[74] D.-K. Yang and S.-T. Wu, *Fundamentals of Liquid Crystal Devices*, Chichester, UK, John Wiley & Sons, 2006.
[75] D. Gennes, P. Gilles, and J. Prost, *The Physics of Liquid Crystals*, Oxford, UK, Clarendon Press, 1993.
[76] I. Kim, M. A. Ansari, M. Q. Mehmood, et al., "Stimuli-responsive dynamic metaholographic displays with designer liquid crystal modulators," *Adv. Mater.*, vol. 32, p. 2004664, 2020.
[77] J. P. Balthasar Mueller, N. A. Rubin, R. C. Devlin, B. Groever, and F. Capasso, "Metasurface polarization optics: independent phase control of arbitrary orthogonal states of polarization," *Phys. Rev. Lett.*, vol. 118, p. 113901, 2017.
[78] M. A. Naveed, M. A. Ansari, I. Kim, et al., "Optical spin-symmetry breaking for high-efficiency directional helicity-multiplexed metaholograms," *Microsyst. Nanoeng.*, vol. 7, p. 5, 2021.
[79] J. Hu, X. Zhao, Y. Lin, et al., "All-dielectric metasurface circular dichroism waveplate," *Sci. Rep.*, vol. 7, p. 41893, 2017.
[80] Z. Ma, Y. Li, Y. Li, Y. Gong, S. A. Maier, and M. Hong, "All-dielectric planar chiral metasurface with gradient geometric phase," *Opt Express*, vol. 26, pp. 6067–6078, 2018.
[81] K.-H. Kim and J.-R. Kim, "Dielectric chiral metasurfaces for second-harmonic generation with strong circular dichroism," *Ann. Phys.*, vol. 532, p. 2000078, 2020.
[82] A. S. Rana, I. Kim, M. A. Ansari, et al., "Planar achiral metasurfaces-induced anomalous chiroptical effect of optical spin isolation," *ACS Appl. Mater. Interfaces*, vol. 12, pp. 48899–48909, 2020.
[83] Z. Li, W. Liu, H. Cheng, D.-Y. Choi, S. Chen, and J. Tian, "Spin-selective full-dimensional manipulation of optical waves with chiral mirror," *Adv. Mater.*, vol. 32, p. 1907983, 2020.

Supplementary Material: The online version of this article offers supplementary material (https://doi.org/10.1515/nanoph-2022-0075).